15th International Symposium on Particle Image Velocimetry – ISPIV 2023
June 19–21, 2023, San Diego, California, USA

High-resolution PIV measurements of the shock boundary layer interaction within a highly loaded transonic compressor cascade

J. Klinner[1*], E. J. Munoz Lopez[2], A. Hergt[2], C. Willert[1]

[1]Institute of Propulsion Technology, Engine Measurement Dept., German Aerospace Center (DLR), Koeln, Germany

[1]Institute of Propulsion Technology, Fan and Compressor Dept., German Aerospace Center (DLR), Koeln, Germany

[*] joachim.klinner@dlr.de

Keywords: time-resolved PIV, POD, SPOD, shock boundary layer interaction, SBLI

Abstract

Both snap-shot as well as time-resolved PIV (TR-PIV) measurements are performed on a transonic compressor cascade to elucidate the underlying shock-boundary layer interaction process. In order to align both the instantaneous passage shock and the boundary layer along with its separation downstream of the shock foot, shadowgraph imagery is acquired synchronous with TR-PIV recordings. Statistics from PIV snapshots reveal that the passage shock fluctuates by up to 13% of the chord. Frequencies of shock motion lay in a range between 500 and 600 Hz with an additional specific tone near 1142 Hz. With TR-PIV, the velocity field in the interaction region is sampled at 20 kHz, which temporally resolves the motion of the shock foot and captures size variations of the separation region. The thickness of the laminar boundary layer (BL) is found to grow as the shock moves downstream. A rapid upstream motion of the shock leads to even higher BL growth rates and large scale flow separation downstream. Proper orthogonal decomposition (POD) of the snap-shot PIV data reveals that 50% of the energy is contained in the first 4 modes. The corresponding POD eigenvalue spectrum exhibits a -11/9 decay slope as predicted in literature for the inertial range of inhomogeneous turbulence.

1 Introduction

In the design of transonic turbomachinery blading, the correct prediction of shock instabilities in terms of strength and position is of great importance in order to properly localize separations, which in turn affect both flow guiding capability and viscous losses, and thus the working range. Furthermore, it is clear that underestimation of the corresponding dynamic pressure loads and inaccurate prediction of the frequency range can have serious consequences for the structural life of the blading. For turbomachinery in particular, there is therefore a great need for experimental data to provide deeper insight and help identify the mechanisms that lead to self-sustaining shock oscillations and, further, to validate loss-limiting measures (e.g. by passive flow control).

In the framework of the TEAMAero (2021) research project sources of unsteadiness of the shock laminar boundary layer interaction (SLBLI) in a non-proprietary transonic cascade TEAMAero (TCTA) Munoz Lopez et al. (2023) are investigated at chord based Reynolds numbers of $1.3 - 1.4 \times 10^6$ and inlet Mach numbers of 1.05 and 1.22. In addition to mechanisms that can govern shock oscillations on a single airfoil, i.e. wave propagation feedback or global aerodynamic mode instabilities (for a review see Giannelis et al. (2017)), for cascade flows inter-passage coupling of shock unsteadiness occurs, for example due to oscillating bow shocks emanating from the leading edges of adjacent blade passages.

Standard PIV with a high dynamic spatial range of 100:1 (in the following referred to as high spatial range PIV (HR-PIV)) was performed to measure flow velocities below and above the shock foot to

capture shock induced separations and corresponding shock patterns. Based on this data, the snapshot proper orthogonal decomposition (POD) method (Sirovich, 1987)is employed with the intention to provide a reduced-order model of the laminar shock boundary layer interaction (SBLI) on the basis of large sets of spatial highly resolved PIV samples. The decomposition of the random vector fields into a set of deterministic functions (i.e. orthogonal spatial modes) may allow the assignment of spatially correlated structures that represent a large fraction of the velocity fluctuations in the SBLI zone. The hope is that a limited number of these spatial modes can provide further insights in the organization of the flow.

Current literature provides only a limited number of publications on the analysis of experimental data of SBLIs based on snapshot POD. Mustafa et al. (2019) analyzed velocity fluctuations from krypton tagging velocimetry in a compression-corner shock-turbulent boundary layer interaction (BLI) and found the first POD modes are responsible for features such as separation bubble filling, collapse and oscillation. Cottier et al. (2019) and Hoffman et al. (2022) analyzed high-speed Schlieren images of cylinder-induced SBLI in a Mach 6 wind tunnel using both POD and as well as spectral proper orthogonal decomposition (SPOD) and dynamic mode decomposition (DMD) concluding that the lower order modes represent coherent structures in the shock patterns such as the flow separation beneath the lambda-shock structure.

The advantage of using SPOD analysis over the snapshot POD, is that SPOD can recover spatio-temporal coherent structures and thus might be more suitable for the analysis of experimental data of SBLIs in transonic compressor or turbine flows, given that these flows are known to exhibit characteristic frequency bands or peaks in the power spectral density (PSD) (Klinner et al., 2021; Munoz Lopez et al., 2023). The previous studies indicated frequency locked oscillations of shock and separation bubble that recently also have been captured in numerical studies based on large eddy simulation (LES) (Klose et al., 2023; Hergt et al., 2023).

However, providing both spatially and temporally high-resolution PIV samples in compressor cascade flows at relevant operation conditions reaches the limits of current camera technology which allow frame rates of $50 - 80$ kHz maximum at square image sizes of 1 MPixel. At the same time, tracking of the fastest structures with an adequate spatial resolution at maximum velocities exceeding 400 m/s would require frame rates in the megahertz range.

By reducing image dimension to a few hundred pixels combined with the use of frame straddling allows to reliably capture the flow field below the shock foot and in the downstream shear layer at sampling rates in 50 kHz range (Klinner et al., 2021). For the TCTA at aerodynamic design point (ADP), Fig. 3 indicates the region which can be captured by high speed cameras available in this project running at frame rates of 40 khz. To correlate the high-speed PIV (HS-PIV) flow field data with the passage shock motion, simultaneously acquired high-speed shadowgraph imaging locates either the upstream bow shock or shock foot position above the SBLI.

In the following, the experimental setups for the combined shadowgraph visualization and flow field measurement by means of HR-PIV and HS-PIV are described, followed by a preliminary analysis of the acquired snapshot POD data.

2 Experimental methods and data processing

2.1 Description of the cascade model and test rig

The compressor blade cascade (cf. Table 1) consists of 6 blades of 100 mm chord length and 168 mm span whose non-proprietary geometry is representative of a transonic section from a modern compressor rotor. The in-house design process and CFD based optimization was aimed at minimizing the losses at the design point and over the working range while maintaining representative aerodynamic blade loadings Munoz Lopez et al. (2023).

The cascade is operated in the transonic cascade wind tunnel of the DLR Insitute of Technology (cf. Fig. 1) which is a closed loop, continuously running facility with a rectangular supersonic nozzle and a variable test section through adjustment of the lower end wall. Side-wall suction of the windtunnel enables the control of the sidewall BLs and is set to an axial velocity density ratio (AVDR) near unity to ensure that shock systems exhibit minimal curvature in span-wise direction.

2.2 Image acquisition setup and PIV evaluation

To first localize the SBLI region in the center passage of the cascade during commissioning, conventional 2D-2C PIV is conducted with the measurement plane located at mid-span. The double-frame camera

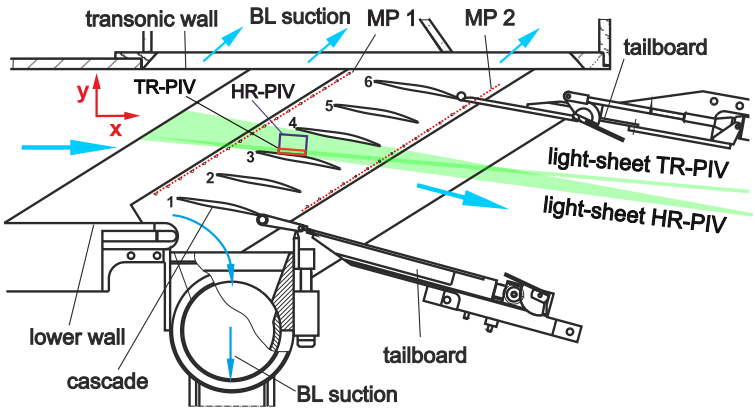

Figure 1: Test section of the cascade windtunnel and measurement stations for TR-PIV and HR-PIV

Table 1: Cascade design and flow parameters

Blade chord length	c	= 100.0 mm
Cascade pitch	t	= 65 mm
Stagger angle	β_{st}	= 135.8°
Inlet Mach number ADP / ODP	Ma_1	= 1.20 / 1.05
Chord based Reynolds number	Re	$\approx 1.3 - 1.4 \times 10^6$
Inlet flow angle	β_1	= 146.4°
Flow turning angle	$\beta_1 - \beta_{st}$	= 10.6°
Blade span	h	= 168 mm

(ILA.sCMOS, 2560 × 2160 pixel) is equipped with an Nikkor Micro $f = 200$ mm lens at f#5.6 and captures image pairs at 25 Hz. For the global overview the magnification was set to 0.21 or 30.5 µm/pixel and 5000 particle images were captured in two different field of view (FOV)s, either covering the upstream bow shock at the leading edge and SBLI region or the flow near the pressure side of the blade above.

The second PIV setup provides sequences of up to 15000 particle images at a smaller FOV of 33 × 28 mm^2 covering parts the SBLI region and the upstream boundary layer at a magnification of 0.50 or 13.0 µm/pixel. The FOV is highlighted in cf. Fig. 1 and Fig. 3. With the dynamic spatial range (DSR) exceeding 100 (Adrian, 1997), the measurements are referred to as HR-PIV in the following. The laser light sheet is introduced through a rigid, air-purged light-sheet probe that is positioned about 500 mm downstream from the FOV. Tracer illumination is provided by a Nd:YAG double pulse (Evergreen, Lumibird) laser running at a double-pulse rate of 25 Hz and a pulse energy of 100 mJ.

Dense smoke oil-based seeding provided by a smoke generator (Vicount) is injected into the settling chamber upstream of the test section. A centrifugal pump facilitates aerosol sizes < 1 µm.

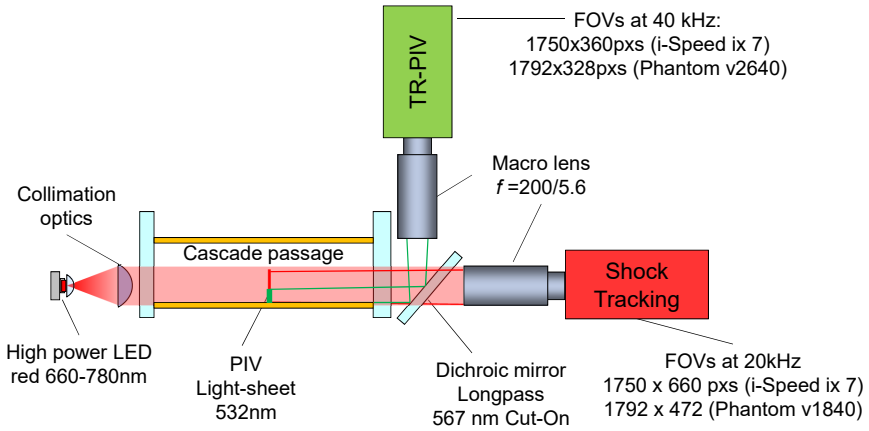

Figure 2: Combined optical setup for high-speed PIV and shadowgraph visualizations

To process the PIV recordings, image enhancement is applied to improve particle image contrast which increases the data validation rate in the subsequent cross-correlation analysis. Here, a minimum intensity image calculated from each image sequence is subtracted followed by a clipping of intensities above 98% of the cumulative intensity range. Using coarse-to-fine PIV processing algorithm with a final interrogation window size of 24×24 pixels (0.31×0.31 mm^2) achieves validation rates of 98%. A drop in the validation rates within the laminar boundary layer and separation region is due to significantly lower particle image densities in these regions (Klinner et al., 2021). The corresponding validation scheme is based on normalized median filtering with a threshold of 4.0 Westerweel and Scarano (2005). The DSR of these measurements, defined as the ratio of image width and smallest resolvable spatial variation, is in the order of 100:1. All particle images were evaluated using commercial software (PIVview 3.9) and an in-house Python-based PIV package for batch processing.

For time resolved PIV (TR-PIV), upstream velocities of up to 400 m/s require the use of a double-pulse high speed laser system, which can provide pulse separations between $1-1.2$ µs at repetition rates exceeding f_s=20 kHz. Previous studies on the TCTA with high speed schlieren have shown that the frequency band of the fluctuations of the near normal shock position ends below 10 kHz (Munoz Lopez et al., 2023). Therefore, the image acquisition rate for TR-PIV was set at 40 kHz (20 kHz double-frame rate).In the present configuration, tracers can be detected at a doubled light sheet height (4 mm rather than 2 mm previous TR-PIV campaigns), which allows the capture of large unsteady separation of the boundary layer (BL) and the growth of the shear layer. With the image magnification set near unity, the TR-PIV setup provides 2D-2C data with the measurement plane located at mid-span of the central cascade passage. Tracer illumination is provided with a high-repetition laser system consisting of a pair of diode pumped solid state lasers (Innolas Photonics, Nanio Air 532-10-V-SP), each providing an average power of up to 10 W (Klinner et al., 2021).

During the commissioning phase HS-PIV recordings were acquired with a high-speed camera (ispeed 726R, iX-Cameras) equipped with a macro lens (Nikon, Nikkor Micro f200/4) at a magnification of 18.5 µm/pixel ($m = 0.73$). At a frame rate of 40 kHz the high-speed camera was operated at a reduced image size of 1750×360 pixel, which corresponds to an image area of 32.3×6.7 mm^2. The reduced FOV is highlighted in Fig. 1.

Fig. 2 shows the combined setup for simultaneous shock tracking by shadowgraphs using high-power LEDs (Willert et al., 2012) which provide frame-synchronized pulses of 2µs width at 20 kHz. The upper edge of the image area is about twice as far away from the suction side as for TR-PIV allowing to also capture oscillations of the shock pattern above the separation. Equipped with a Nikkor Micro 200/5.6 lens, the shadowgraph camera images a FOV of 18.7x14 mm^2 at an image scale of 23 µm/pixel ($m = 0.59$).

In the course of the initial measurements, however, it became apparent that the high-speed camera used for PIV was too insensitive to sufficiently resolve particles in the separation bubble. The upgrade to a more sensitive camera could only be done recently, such that the evaluation and corresponding analysis of the TR-PIV data could not be included in this paper.

3 Results

3.1 Overview of the velocity field in the TCTA

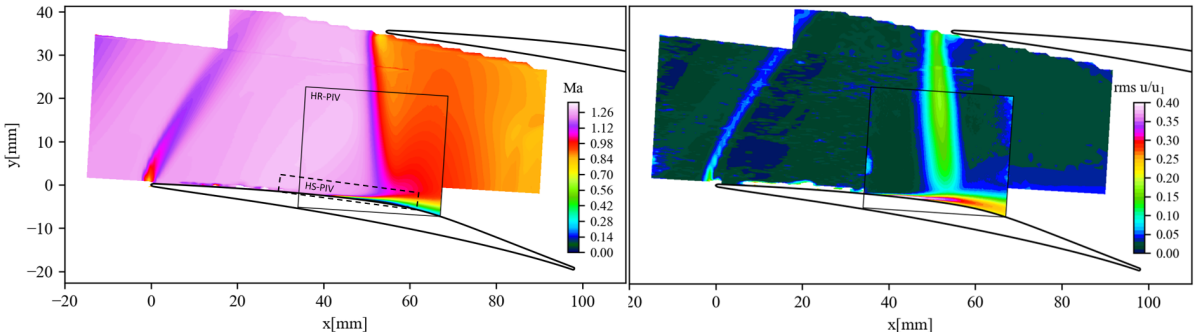

Figure 3: Mean flow field combined of PIV in three measurement regions at the ADP; left: isentropic Mach number, right: rms of u component

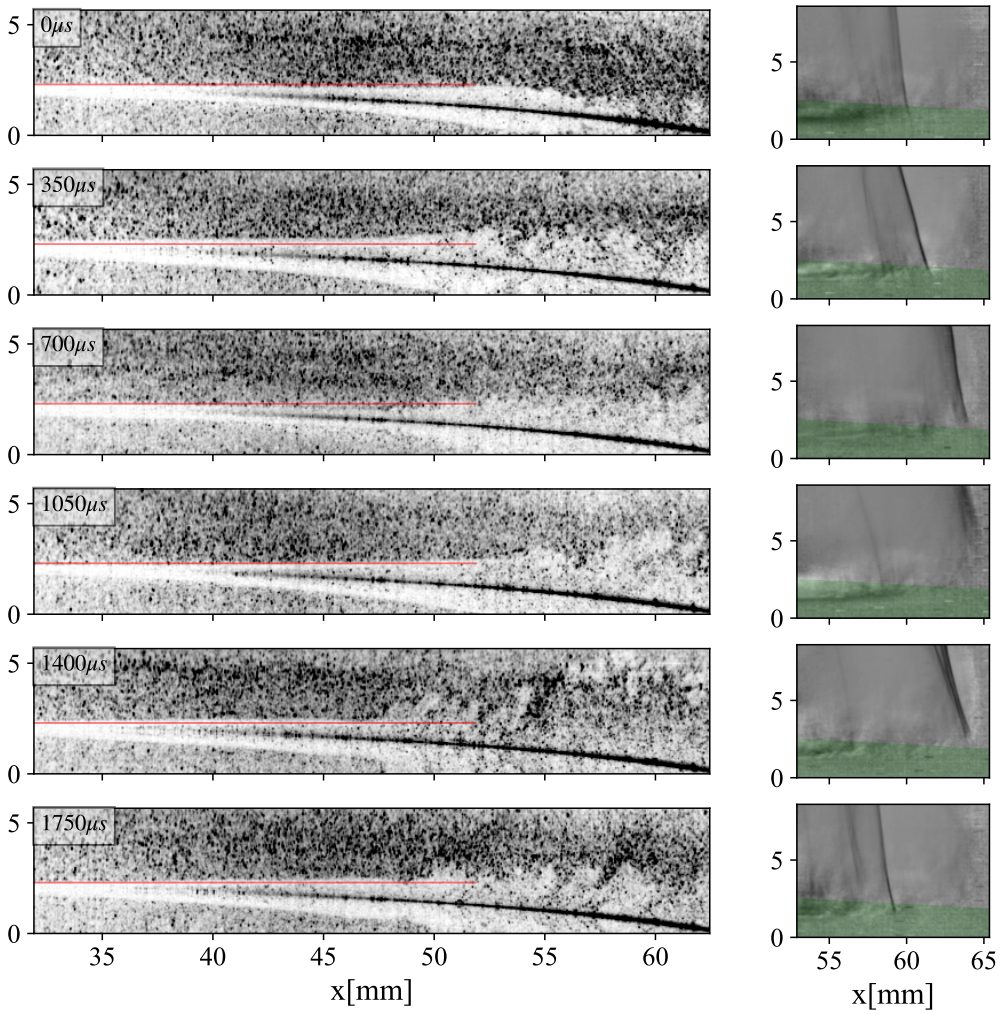

Figure 4: High speed TR-PIV image sequence (left) and simultaneous shadowgraphs (right) composed of every 14th particle image and every 7th shadowgraph (2.875kHz),the red line indicates the laminar BL thickness in the first frame, the green region indicates the light-sheet position

Fig. 3, left, provides an overview of the mean isentropic Mach number at mid-span between two neighbouring blades at the ADP and is compiled from three different regions including the HR-PIV data. The leading edge of the upper blade causes a bow shock which on the pressure side is being intensified and crosses the passage impinging on the suction side of the blade below. Fig. 3, right, exhibits a significant rise of the axial component within the passage to levels up to 20% which is associated with increased shock vibrations in this area. From shock detections in up to 15 000 PIV snapshots it could be determined that these high fluctuations are primarily caused by fluctuations of the shock position by up to 13% of chord. Aside from the fluctuations within the passage, the highest dynamics are present below the shock foot where the flow separates and a shear layer is being formed.

The intermittent character of the separation region and the unsteadiness of the shock position is visualized in Fig. 4 by a sequence of six time resolved particle images with corresponding shock shadowgraphs. The different particle density between laminar boundary layer and the outer flow allow visualization of the growth and separation of the laminar boundary layer followed by the formation of the shear layer. The red line approximates the thickness of the laminar BL in the first frame (cf. Fig. 4 top). The image series clearly indicates that the thickness of the laminar BL varies upstream of the shock position. Also, the shear layer grows during the downstream movement of the shock. During the faster upstream movement of the shock shown in the last three frames the laminar BL grows even more significantly.

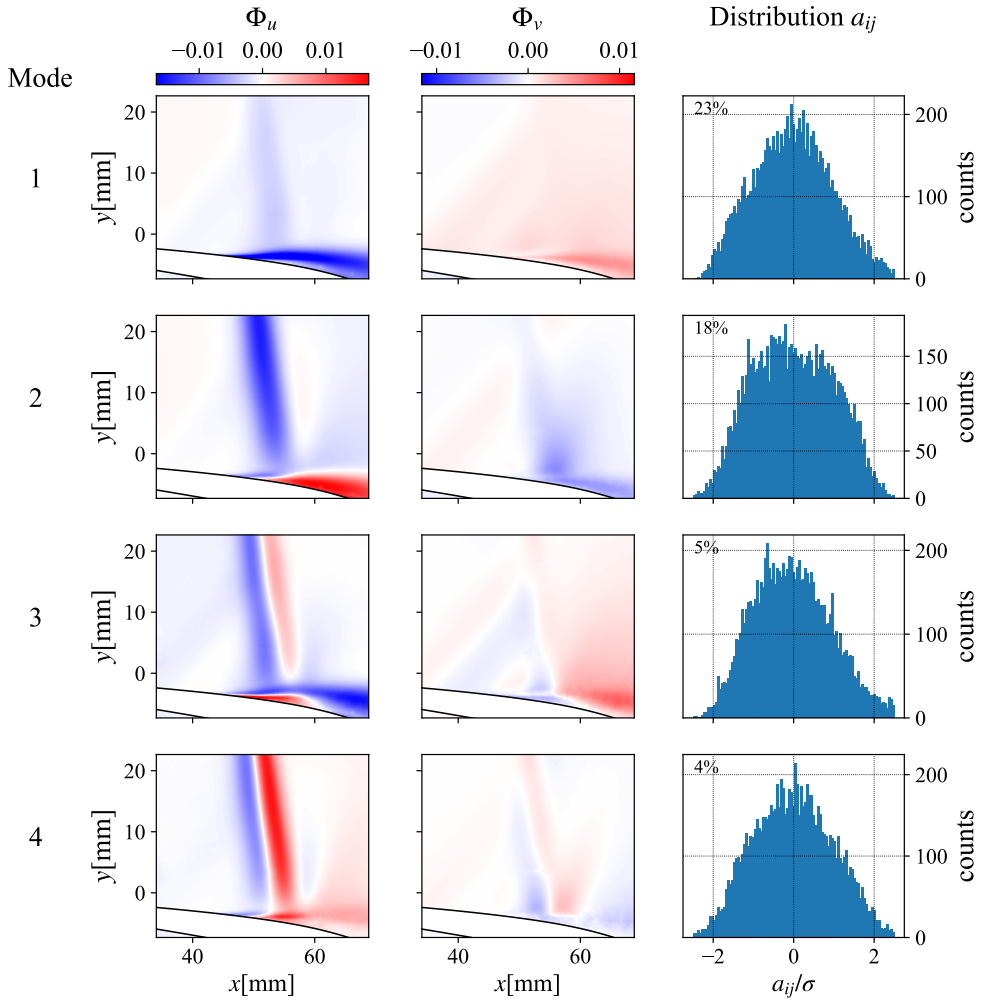

Figure 5: Spatial modes in the SBLI region (u (left) and v (middle)) and distributions of time coefficients $a_{i,j}$ (right) which were used to identify characteristic structures for each mode; the energy content per mode is provided in percent in the top left corner of each histogram.

3.2 Modal decomposition results

3.2.1 POD evaluation

POD is applied to the fluctuating velocities measured by HR-PIV in the hope of revealing spatially coherent structures near the shock foot. Since these data series were recorded at 25 Hz sampling, it can be assumed that they are statistically independent. The random vector field is decomposed into a set of orthogonal spatial modes $\phi_j(\mathbf{x}_n)$ weighted by the time coefficients a_{ij} so that:

$$\mathbf{u'_i}(\mathbf{x}_n) = \sum_{j=1}^{N} a_{ij}\,\phi_j(\mathbf{x}_n) \tag{1}$$

The matrix $\mathbf{u}'(\mathbf{x_i}_n)$ consists of $m = 10000$ snapshots while each vector field consists of $179 \times 212 = N_y \times N_x = n = 37948$ vectors $(u-\overline{u}, v-\overline{v})$. In addition, a decomposition of the fluctuating vorticity component $\omega_z - \overline{\omega_z}$, obtained by applying a second order accurate central differences scheme on the velocity field data.

To speed up the POD solving, the eigenvalues and eigenvectors were calculated using the snapshot technique (Sirovich, 1987; Weiss, 2019) instead of the direct method, i.e., by processing an $m \times m$ rather than $n \times n$ correlation matrix. Python based POD was implemented by the principal component analysis (PCA)

routines included in the scikit-learn package (Pedregosa et al., 2011) which use the LAPACK solver for the singular value decomposition.

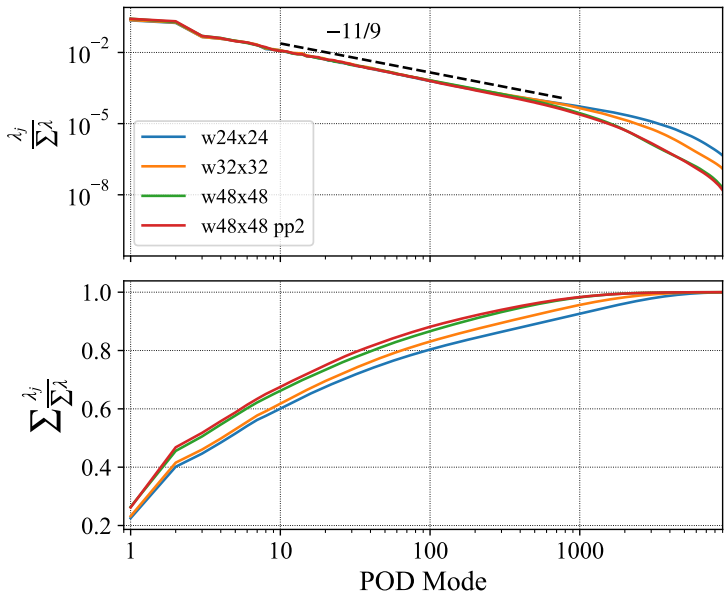

Figure 6: Fraction of variance per mode (top) and cumulative fraction of variance (bottom), the dashed line corresponds to the mode number raised to the $-11/9$ power as proposed by Knight and Sirovich (1990)

3.2.2 Description and interpretation of POD results

The 2D-2C HR-PIV data consisting of up to 10 000 snap-shots is decomposed into principal modes by the aforementioned snap-shot POD method. The 4 most energetic modes are plotted in Fig. 5 and clearly identify the characteristic flow features and regions were the velocity fluctuations, i.e. differences with respect to the mean velocity, are correlated.

The corresponding modal energy spectrum exhibits a $-11/9$ decay slope across more than 3 decades (cf. Fig. 6). This slope is predicted for the inertial range by Knight and Sirovich (1990) and is related to the classical $k^{-5/3}$ energy decay rate of isotropic inertial-range turbulence but extended to inhomogeneous inertial turbulence. Similar observations have already been reported for experimental data by Kaffel et al. (2016); Mustafa et al. (2019). Deviations from the $-11/9$ slope appear for mode numbers larger than 1000 and indicate a higher energy content for smaller interrogation windows which could either indicate a higher noise level or a reduced filtering of smaller structures.

To gain insight into the flow features represented by the first four modes, similar to that described in Mustafa et al. (2019), HR-PIV snapshots were sought whose time coefficients $|a_{ij}|$ are greater than 1.8σ, where σ is the standard deviation of time-coefficients for each individual mode (based on the distributions shown in Fig. 5). Shown at the top of Fig. 7 is the mean isentropic Mach number determined from 10 000 samples. Below, for each snapshot the Mach number and the deviation from the mean velocity field (i.e. the POD input) are shown side-by-side in Fig. 7. The two plots on the left correspond to snapshots with particularly large time coefficients ($a_{ij} > 1.8\sigma$) for the respective mode, while the two plots on the right correspond to negative time coefficients where $a_{ij} < -1.8\sigma$. Snapshots associated with the first mode (top row in Fig. 7) have the following characteristics: The shock is at its mean position and either a large separation occurs for $a_{ij} > 1.8\sigma$, indicated by a large velocity deficit, or the flow is attached with no separation visible ($a_{ij} < -1.8\sigma$). From this, it can be reasoned that for the first spatial mode (Fig. 5, top row), the velocities in the separation region fluctuate together toward lower or higher velocities, indicating that the separation zone is either very large or almost nonexistent (flow is attached). At its center position, the shock front is likely to rapidly move upstream or downstream frequently, resulting in the highest or lowest relative velocities and pre-shock Mach numbers, which is accompanied by large variations in the extent of the separation region.

The second spatial mode (Fig. 5, second row) becomes apparent through the following feature in the corresponding PIV snapshots (second row in Fig. 7): either the shock is located upstream of its mean position and the flow is attached ($a_{ij} > 1.8\sigma$) or the shock is positioned downstream of the mean position and separation occurs ($a_{ij} < 1.8\sigma$). It seems that the shock begins to move upstream or downstream, so

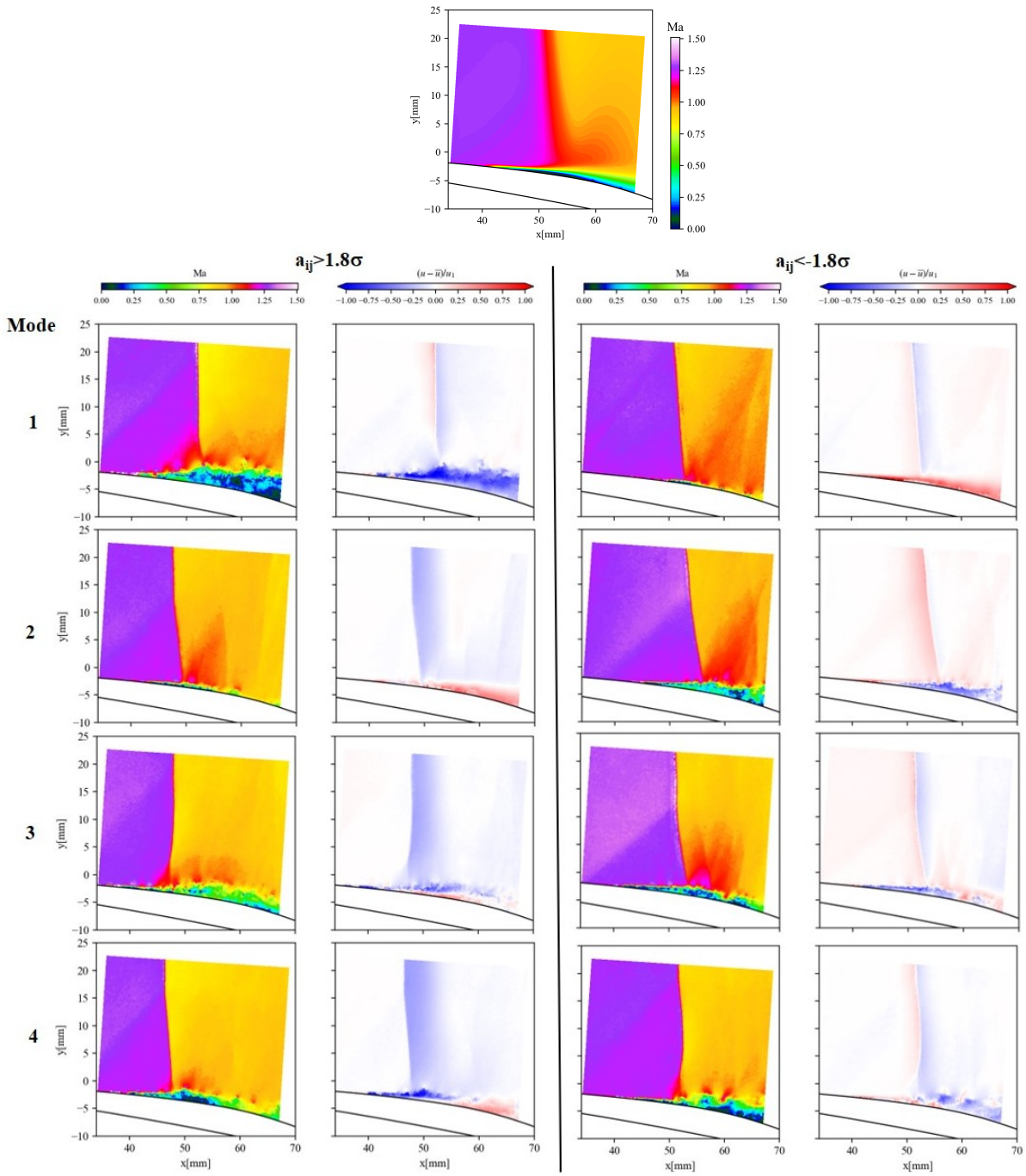

Figure 7: Mean flow field from HR-PIV (Top) and PIV snapshots which are representatives of the POD modes 1 (first row) to 4 (bottom row) based on very large $a_{i,j} > 1.8\sigma$ (left) or very small time-coefficients $a_{i,j} < -1.8\sigma$ (right); per snapshot Mach numbers and deviation of the axial velocity from the mean are plotted side-by-side.

that the resulting velocity upstream of the shock is slightly above or below the mean, resulting in smaller variations in the size of the separation region than in the first mode.

The third spatial mode (Fig. 5, third row) shows a complementary picture to the second mode also with respect to the transverse component downstream of the shock (Fig. 5, second column). In addition, the region below and downstream of the shock foot is divided into smaller regions of positive (momentum

surplus) and negative correlation (momentum deficit) which are stacked in the transverse direction. This is also reflected in the occurrence of small-scale structures in the separation region in the snapshots shown in the third row in Fig. 7.

The complex nature of the spatial modes obtained from POD of statistically independent samples requires further analysis by making use of the time-resolved PIV data and accompanying shock tracking. This would provide information on the corresponding direction and velocity of shock motion and permits the additional correlation with the size and location of the associated flow separation.

4 Conclusions and outlook

Both snap-shot and time-resolved PIV measurements are performed on the non-proprietary DLR transonic compressor cascade (TCTA) to elucidate the underlying shock-boundary layer interaction process at an inlet Mach number up to 1.20. To align both the shock motion and the boundary layer and its separation downstream of the shock, shadowgraphs of the shock system are acquired synchronously with TR-PIV images. Statistics of the PIV snapshots indicate that the passage shock fluctuates by up to 13% of the chord. With TR-PIV, the velocities in the interaction region are sampled at 20 kHz, which temporally resolves the motion of the shock foot and the size variations of the separation region. The thickness of the laminar boundary layer (BL) is found to grow as the shock moves downstream. A rapid upstream motion of the shock leads to even higher BL growth rates and large scale flow separation downstream.

Proper orthogonal decomposition (POD) of the snap-shot PIV data reveals that 50% of the energy is contained in the first 4 modes. The corresponding POD eigenvalue spectrum exhibits a -11/9 decay slope as predicted in literature for the inertial range of inhomogeneous turbulence. The first spatial mode contains 23% of the total fluctuations that essentially lead to the filling and collapse of the separation bubble, and thus presumably corresponds to the fastest shock motions and thus the highest and lowest Mach numbers before the shock. For the second mode with 18% of the total energy, the shock is outside its mean position, and the separation region tends to be smaller, presumably associated with slower shock motion.

For higher modes the separation region tends to be smaller and the spatial modes show a partitioning of the SBLI region into smaller regions along with a correlation of the axial velocity component.

The interpretation of these dynamical effects will be subject of further analysis using the recently acquired, extensive data sets consisting of time-resolved flow field measurements and shadowgraph imagery.

References

Adrian R J (1997). Dynamic ranges of velocity and spatial resolution of particle image velocimetry. *Measurement Science and Technology* 8(12):1393. doi:10.1088/0957-0233/8/12/003. URL 10.1088/0957-0233/8/12/003

Cottier S, Combs C S, and Vanstone L (2019). Spectral Proper Orthogonal Decomposition Analysis of Shock-Wave/Boundary-Layer Interactions. In *AIAA Aviation 2019 Forum*. American Institute of Aeronautics and Astronautics, Dallas, Texas. doi:10.2514/6.2019-3331. URL 10.2514/6.2019-3331

Giannelis F N, Vio A G, and Levinski O (2017). A review of recent developments in the understanding of transonic shock buffet. *Progress in Aerospace Sciences* 92:39 – 84. doi:10.1016/j.paerosci.2017.05.004. URL http://www.sciencedirect.com/science/article/pii/S0376042117300271

Hergt A, Klose F B, Klinner J, Bergmann M, Hergt A, Munoz Lopez E, Grund S, and Morsbach C (2023). On the shock boundary layer interaction in transonic compressor blading. In *Proceedings of the ASME Turbo Expo*. American Society of Mechanical Engineers, Boston. Accepted

Hoffman E N A, Rodriguez J M, Cottier S M, Combs C S, Bathel B F, Weisberger J M, Jones S B, Schmisseur J D, and Kreth P A (2022). Modal Analysis of Cylinder-Induced Transitional Shock-Wave/Boundary-Layer Interaction Unsteadiness. *AIAA Journal* 60(5):2730–2748. doi:10.2514/1.J060880. URL https://arc.aiaa.org/doi/10.2514/1.J060880

Kaffel A, Moureh J, Harion J L, and Russeil S (2016). Tr-piv measurements and pod analysis of the plane wall jet subjected to lateral perturbation. *Experimental Thermal and Fluid Science* 77:71–90. doi:https://doi.org/10.1016/j.expthermflusci.2016.04.001. URL https://www.sciencedirect.com/science/article/pii/S0894177716300772

Klinner J, Hergt A, Grund S, and Willert C E (2021). High-Speed PIV of shock boundary layer interactions in the transonic buffet flow of a compressor cascade. *Experiments in Fluids* 62(3). ISSN 14321114. doi:10.1007/s00348-021-03145-3. URL https://doi.org/10.1007/s00348-021-03145-3

Klose F B, Morsbach C, Bergmann M, Hergt A, Klinner J, Grund S, and Kügler E (2023). a numerical test rig for turbomachinery flows based on large eddy simulations with a high-order discontinuous Galerkin scheme - part 2: shock-capturing and transonic flows. In *Proceedings of the ASME Turbo Expo*. American Society of Mechanical Engineers, Boston. Accepted

Knight B and Sirovich L (1990). Kolmogorov inertial range for inhomogeneous turbulent flows. *Physical Review Letters* 65(11):1356–1359. doi:10.1103/PhysRevLett.65.1356. URL https://link.aps.org/doi/10.1103/PhysRevLett.65.1356

Munoz Lopez J E, Hergt A, Klinner J, Grund S, Karboujian J, and Flamm J (2023). New insights into the mechanisms of unsteady shock-boundary layer interaction. In *Proceedings of the ASME Turbo Expo*. American Society of Mechanical Engineers, Boston. Accepted

Mustafa M A, Parziale N J, Smith M S, and Marineau E C (2019). Amplification and structure of streamwise-velocity fluctuations in compression-corner shock-wave/turbulent boundary-layer interactions. *Journal of Fluid Mechanics* 863:1091–1122. doi:10.1017/jfm.2018.1029. URL https://doi.org/10.1017/jfm.2018.1029

Pedregosa F, Varoquaux G, Gramfort A, Michel V, Thirion B, Grisel O, Blondel M, Prettenhofer P, Weiss R, Dubourg V, Vanderplas J, Passos A, Cournapeau D, Brucher M, Perrot M, and Duchesnay E (2011). Scikit-learn: Machine learning in Python. *Journal of Machine Learning Research* 12:2825–2830. URL https://www.jmlr.org/papers/v12/pedregosa11a.html

Sirovich L (1987). Turbulence and the dynamics of coherent structures part iii: dynamics and scaling. *Quarterly of Applied Mathematics* 45(3):583–590. doi:10.2307/43637459. URL http://www.jstor.org/stable/43637459

TEAMAero (2021). Towards Effective Flow Control and Mitigation of Shock Effects in Aeronautical Applications (https://h2020-teamaero.eu). URL https://h2020-teamaero.eu

Weiss J (2019). A Tutorial on the Proper Orthogonal Decomposition. In *AIAA Aviation 2019 Forum*. American Institute of Aeronautics and Astronautics, Dallas, Texas. doi:10.2514/6.2019-3333. URL https://arc.aiaa.org/doi/10.2514/6.2019-3333

Westerweel J and Scarano F (2005). Universal outlier detection for piv data. *Experiments in Fluids* 39(6):1096–1100. doi:10.1007/s00348-005-0016-6. URL http://dx.doi.org/10.1007/s00348-005-0016-6

Willert C E, Mitchell D M, and Soria J (2012). An assessment of high-power light-emitting diodes for high frame rate schlieren imaging. *Experiments in Fluids* 53(2):413–421. doi:10.1007/s00348-012-1297-1. URL http://link.springer.com/10.1007/s00348-012-1297-1